

## Two-Dimensional Sixteen Channel Transmit/Receive Coil Array for Cardiac MRI at 7.0 T: Design, Evaluation, and Application

Christof Thalhammer, Dipl-Phys,<sup>1</sup> Wolfgang Renz, PhD,<sup>1,2</sup> Lukas Winter, Dipl-Ing,<sup>1</sup> Fabian Hezel, Dipl-Inf,<sup>1</sup> Jan Rieger, MSc,<sup>1,3</sup> Harald Pfeiffer, Dipl-Ing,<sup>1,4</sup> Andreas Graessl, Dipl-Ing,<sup>1</sup> Frank Seifert, PhD,<sup>1,4</sup> Werner Hoffmann, PhD,<sup>1,4</sup> Florian von Knobelsdorff-Brenkenhoff, MD,<sup>1,5,6</sup> Valeriy Tkachenko,<sup>5,6</sup> Jeanette Schulz-Menger, MD,<sup>1,5,6</sup> Peter Kellman, PhD,<sup>7</sup> and Thoralf Niendorf, PhD<sup>1,3,6\*</sup>

**Purpose:** To design, evaluate, and apply a 2D 16-channel transmit/receive (TX/RX) coil array tailored for cardiac magnetic resonance imaging (MRI) at 7.0 T.

**Materials and Methods:** The cardiac coil array consists of two sections each using eight elements arranged in a  $2 \times 4$  array. Radiofrequency (RF) safety was validated by specific absorption rate (SAR) simulations. Cardiac imaging was performed using 2D CINE FLASH imaging,  $T_2^*$  mapping, and fat–water separation imaging. The characteristics of the coil array were analyzed including parallel imaging performance, left ventricular chamber quantification, and overall image quality.

**Results:** RF characteristics were found to be appropriate for all subjects included in the study. The SAR values derived from the simulations fall well within the limits of legal guidelines. The baseline signal-to-noise ratio (SNR) advantage at 7.0 T was put to use to acquire 2D CINE images of the heart with a very high spatial resolution of  $(1 \times 1 \times 4) \text{ mm}^3$ . The proposed coil array supports 1D acceleration factors of up to  $R = 4$  without significantly impairing image quality.

**Conclusion:** The 16-channel TX/RX coil has the capability to acquire high contrast and high spatial resolution images of the heart at 7.0 T.

**Key Words:** ultrahigh field MRI; cardiovascular MRI; transceiver array; parallel imaging

**J. Magn. Reson. Imaging 2012;36:847–857.**

© 2012 Wiley Periodicals, Inc.

CARDIAC MAGNETIC RESONANCE IMAGING (CMR) is an area of vigorous research driven by a growing spectrum of CMR indications (1). The intrinsic gains in signal-to-noise ratio (SNR) and contrast-to-noise ratio (CNR) are the main motivation for moving toward CMR at ultrahigh magnetic fields ( $B_0 \geq 7.0 \text{ T}$ ) (2–8), but several concomitant effects bear the potential to spoil these benefits. Practical obstacles include increased  $B_0$  inhomogeneities due to susceptibility effects, faster  $T_2^*$  decay (9), and severe distortion of the electrocardiogram (ECG) commonly used for cardiac gating/triggering (10,11). Also, constraints dictated by the physics of the applied radiofrequency (RF) fields at higher frequencies ( $\geq 300 \text{ MHz}$ ) constitute a significant challenge for ultrahigh field (UHF) CMR. The short wavelength of the RF fields inside tissue ( $\lambda \approx 12 \text{ cm}$ ) and increased dielectric effects lead to highly complex and nonuniform  $B_1^+$  distributions (12,13) causing shading or local signal dropoff. Local tissue heating due to increased RF power deposition limits the applicable RF power and flip angles. Increased coil and sample related losses can diminish the performance of RF coils at UHF (14).

Various RF coil concepts have been proposed to enable CMR at 7.0 T (4,15–18) including multichannel transmit/receive (TX/RX) coil configurations. Designs for 7.0 T transceiver coil arrays have been typically laid out as 1D arrays, in which the coil elements are arranged along the left–right direction. Modulating  $B_1^+$  along two dimensions has been proven to enhance RF efficiency of a coil array tailored for head imaging (19). Consequently, 2D transceiver arrays with elements also placed along the head–feet direction are natural candidates to further address RF-related obstacles of

<sup>1</sup>Berlin Ultrahigh Field Facility (B.U.F.F.), Max-Delbrueck-Center for Molecular Medicine, Berlin, Germany.

<sup>2</sup>Siemens Healthcare, Erlangen, Germany.

<sup>3</sup>MRI.TOOLS GmbH, Berlin, Germany.

<sup>4</sup>Physikalische-Technische Bundesanstalt (PTB), Germany.

<sup>5</sup>HELIOS Klinikum Berlin-Buch, Department of Cardiology and Nephrology, Berlin, Germany.

<sup>6</sup>Experimental and Clinical Research Center, a joint cooperation between the Charité Medical Faculty and the Max-Delbrück Center for Molecular Medicine, Berlin, Germany.

<sup>7</sup>Laboratory of Cardiac Energetics, National Institutes of Health/NHLBI, Bethesda, Maryland, USA.

\*Address reprint requests to: T.N., Berlin Ultrahigh Field Facility, Max-Delbrueck-Center for Molecular Medicine, Robert-Roessle-Strasse 10, 13125 Berlin, Germany. E-mail: Thoralf.Niendorf@mdc-berlin.de

Received February 8, 2012; Accepted May 7, 2012.

DOI 10.1002/jmri.23724

View this article online at [wileyonlinelibrary.com](http://wileyonlinelibrary.com).

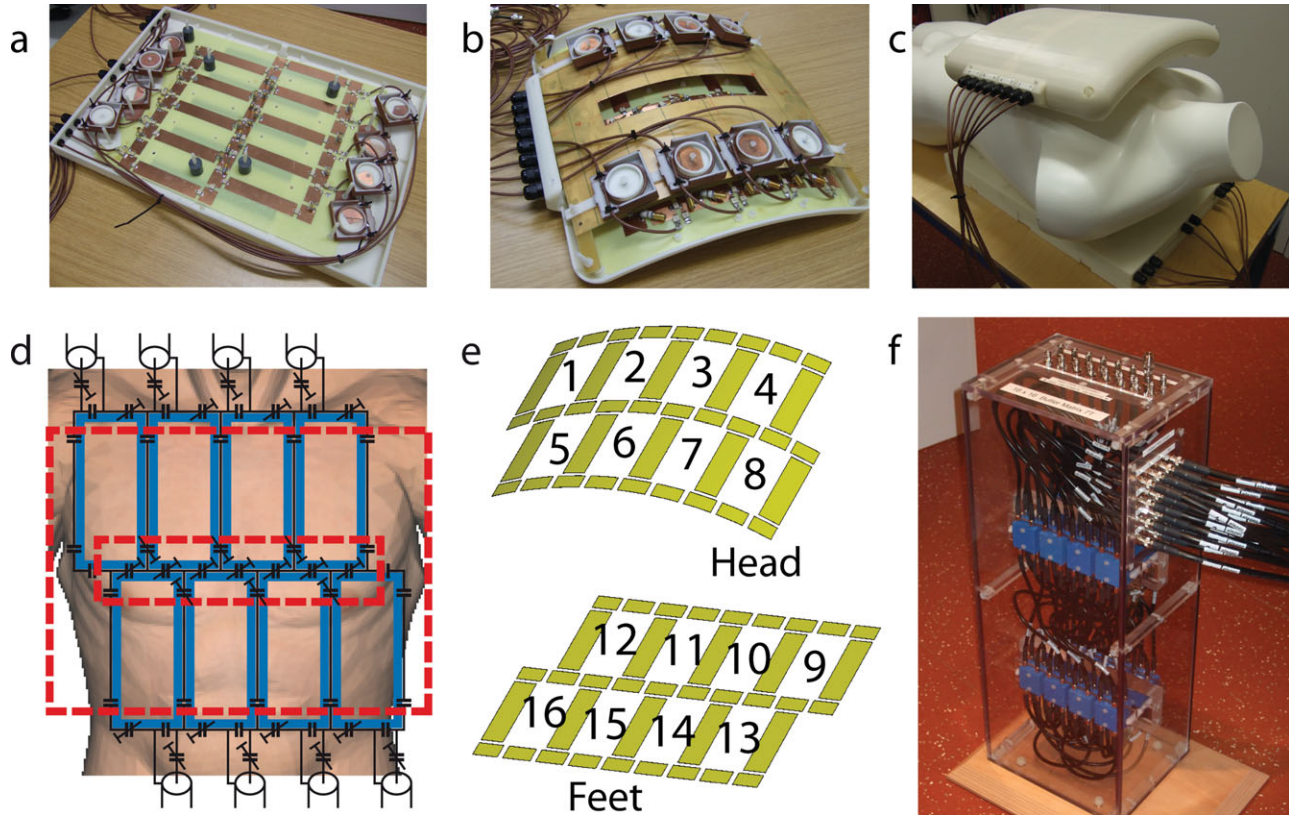


**Figure 1.** (a) Photograph of the posterior section without RF shield. (b) Photograph of the anterior section showing the cable traps mounted behind the RF shield. (c) The coil array placed on a mannequin. (d) Circuit diagram of one section of the 16-channel coil array superimposed to a virtual torso. Coil elements are depicted in blue. The contours of the RF shield are visualized as red dashed lines. A rectangular hole has been cut into the RF shield to enable access to the trim capacitors. (e) Schematic of the coil array identifying the individual elements. (f) Photograph of the custom-built  $16 \times 16$  Butler matrix.

UHF-CMR. Also, it has been predicted that ultrahigh field strengths can allow reduced noise amplification in parallel imaging, which can be used to offset some of the RF power deposition constraints (20,21). Here, 2D RF coil array configurations customized for CMR are of value, due to the heart's position in the chest cavity and the double-oblique orientation of the standard cardiac views used in clinical CMR (22). For all these reasons, this technical development study proposes a 2D 16-channel TX/RX RF coil array that is tailored for CMR at 7.0 T, uses loop elements, and provides image quality suitable for in vivo use, patient comfort, and ease of use. To meet this goal, considerations influencing the coil design and the characteristics of the proposed array are presented in conjunction with specific absorption rate (SAR) simulations. The applicability of the proposed coil design for high-quality and high spatial resolution 2D CINE imaging of the heart at 7.0 T is demonstrated and its suitability for parallel imaging is examined in initial volunteer studies as a precursor to a broader clinical study. The application of the proposed coil for breath-held myocardial  $T_2^*$  mapping and fat-water separation imaging at 7.0 T is demonstrated. The merits and limitations of the 16-channel transceiver array are discussed and implications for cardiac MR at 7.0 T are considered.

## MATERIALS AND METHODS

### Coil Design

Dedicated cardiac TX/RX coil arrays that closely fit the torso are more RF-efficient than body coils for CMR at 7.0 T (23). For sufficient patient comfort and ease of use, the coil array was designed to consist of a planar posterior section (Fig. 1a) integrated into the patient table cushions and a modestly curved anterior section (Fig. 1b) to fit an average torso, as illustrated in Fig. 1c. Loop elements balance  $B_1^+$  depth penetration and SAR (24). Three rectangular loop elements were arranged in a triangular form that allows decoupling of all neighboring elements. This structure can be used as a building block for 2D arrays, as shown in Fig. 1d. Decoupling of adjacent coil elements was achieved by a common conductor and a shared decoupling capacitor. A high number of channels provides increased control over the  $B_1^+$  distribution and supports parallel imaging with modest to high acceleration factors (22). The number of channels is related to the element size via the anatomy of the torso and the desired field of view (FOV). The size of the individual loop elements influences the ratio of unloaded to loaded  $Q$ -factors (25) and mutual coupling via the distance of next-neighboring elements. For both sections of the array an identical arrangement of eight

elements in a  $2 \times 4$  pattern with an element size of  $6 \times 13$  cm (Fig. 1a) was found to meet the needs of whole-heart coverage while balancing element size and number of TX/RX channels. Based on electromagnetic field (EMF) simulations, a conductor width of 2 cm was chosen to balance the competing constraints of  $B_1$  uniformity, ohmic losses, and SAR. An RF shield was placed above the array to reduce radiation losses. It was made of slotted copper foil to minimize eddy currents. Preliminary experiments showed that a gap of 2 cm between the RF shield and the coil array resulted in sufficient decoupling of neighboring and next-neighboring elements for the given layout. The structure depicted in Fig. 1d was etched on a board of FR-4 material. Ceramic capacitors (American Technical Ceramics, Huntington Station, NY) and non-magnetic trim capacitors (Voltronics, Denville, NJ) were placed at the positions indicated in Fig. 1d. A solid casing (Fig. 1a–c) was designed to meet the needs of patient comfort and ease of use using Autodesk Inventor 2010 (San Rafael, CA). The coil casing was constructed with the rapid prototyping system BST 1200es (Dimension, Eden Prairie, MN) using ABSplus material (acrylonitrile butadiene styrene). The casing assured a minimum distance of 1.5 cm between the coil conductors and the tissue in order to prevent excessive tissue heating due to the high electric fields in the close vicinity of the conductors and capacitors. Also, the casing provides safety and comfort since it prevents contact to any electrical conductor of the coil array. One custom-built cable trap per channel was mounted to the coaxial connectors at a distance of 10 cm to the feeding point. Cable traps were designed as single-turn solenoids of the coaxial cable itself with an appropriate capacitor soldered to the outer conductor at the crossing of the cable to achieve an effective reduction of shield currents at 297 MHz. For the anterior section, the cable traps were placed behind the RF shield to avoid coupling with the coil elements. Additionally, all cable traps were shielded individually using copper varnish to further reduce coupling with the coil elements and mutual coupling between cable traps.

### Hardware

The RF characteristics of the coil array were assessed using an 8-channel vector network analyzer ZVT 8 (Rohde & Schwarz, Memmingen, Germany). All images were acquired on a 7.0 T whole-body scanner (Siemens Healthcare, Erlangen, Germany) equipped with an Avanto gradient system (slew rate: 200 mT/m/ms, maximum gradient strength: 40 mT/m; Siemens Medical Solutions, Erlangen, Germany) and an 8 kW RF amplifier (Stolberg HF-Technik, Stolberg-Vicht, Germany).

The output of the RF amplifier was split into 16 equal-intensity signals by means of a home-built  $16 \times 16$  Butler matrix (26) shown in Fig. 1f. The transmit phases of the individual coil elements were adjusted by using the different modes of the Butler matrix (0th/1st-order circular polarized [cp] mode with an increment of  $0/22.5^\circ$  between subsequent output channels) in conjunction with phase shifting coaxial

cables. The coil array was connected to the MR system via a coil interface comprising 16 TX/RX switches and low-noise preamplifiers (Stark Contrasts, Erlangen, Germany).

### Electromagnetic Field Simulations

SAR calculations were performed to estimate the maximum RF power levels possible without putting the subject at risk following the measures presented (17,18). These calculations were based on EMF simulations using the Finite Integration Technique (CST Studio Suite 2010, Darmstadt, Germany) and included an accurate model of the RF coil array, the magnet bore including the RF shield of the gradient coils, and a body model ("Duke") from the Virtual Family (IT'IS Foundation, Zurich, Switzerland) (27). The basic mesh resolution of  $(2 \times 2 \times 2)$  mm<sup>3</sup> was locally refined to model electrical connections on the curved geometry accurately. For rapid tuning, matching, and decoupling of the 16 channels, the corresponding capacitors were modeled as 50  $\Omega$  ports. The results of the 3D simulations were postprocessed using an RF circuit simulator (Design Studio, part of CST Studio Suite 2010) as described (28). SAR values were calculated for all phase settings used in the volunteer studies. The EMF simulations were validated against MR measurements using an elliptical phantom filled with a dielectric liquid ( $\epsilon_r = 57.8$ ,  $\sigma = 0.78$  S/m). For this, relative  $B_1^+$  distributions of the individual coil elements derived from the EMF simulations were compared to  $B_1^+$  maps acquired with the double angle method (29).

### Volunteer Studies

In vivo cardiac imaging was performed using a 2D CINE spoiled gradient echo (FLASH) sequence (breath-hold scan, TE = 2.8 msec, slice thickness = 4 mm, receiver bandwidth = 444 Hz/pixel, 30 phases per cardiac cycle, 8 views per segment). Standard cardiac views (short-axis, two-chamber, three-chamber, and four-chamber view) were acquired using in-plane spatial resolutions of  $(1 \times 1)$  mm<sup>2</sup> and  $(1.4 \times 1.4)$  mm<sup>2</sup> with corresponding TR values of 5.4 msec and 6.3 msec. The nominal flip angle was set to  $35^\circ$  ( $U_{ref} = 400V$ ) to achieve clinically acceptable myocardium/blood contrast. Realizing the constraints of conventional ECG at 7.0 T, an MR-stethoscope (EasyACT, MRI.TOOLS, Berlin, Germany) was used for retrospective gating (11,30).

The imaging sequence included a noise prescan that was used for the measurement of the noise-correlation matrix. The applicability of the coil array for parallel imaging was examined for reduction factors of  $R = 1$  (no reduction),  $R = 2$ ,  $R = 3$ ,  $R = 4$  using generalized autocalibrating partially parallel acquisition (GRAPPA) (self-calibration, 24 reference lines) and sensitivity encoding (SENSE) reconstruction. Optimal noise weighted combining was achieved by means of noise prewhitening calculated from the noise correlation matrix (31). Quantitative SNR and geometry factor (g-factor) maps were calculated (31) from datasets

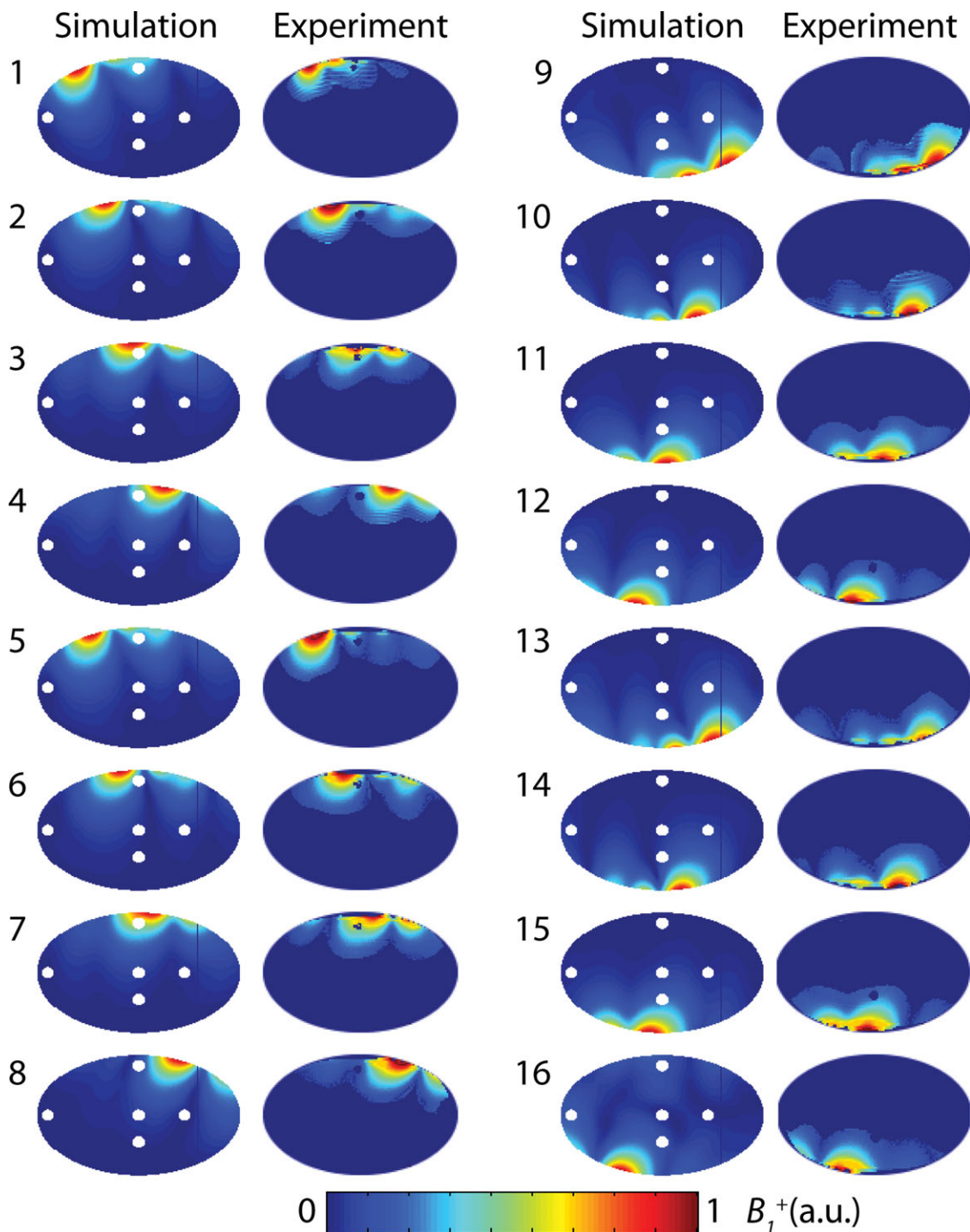


**Figure 2.** Comparison of simulated and experimental  $B_1^+$  distributions in a phantom for all 16 coil elements. The phantom contains cylindrical cavities filled with air, which appear as white circles in the simulated  $B_1^+$  distributions.

of short-axis views with an in-plane resolution of  $(1.4 \times 1.4) \text{ mm}^2$ . For assessment of the parallel imaging performance, the SNR within a region of interest (ROI) covering the left ventricular blood pool was averaged. The mean SNR within the myocardium was subtracted from these results to obtain a blood/myocardium CNR estimate. Geometry factors were analyzed for an elliptical ROI covering the heart.

For  $T_2^*$  mapping of the left ventricle a prospectively triggered spoiled 2D gradient echo technique (slice thickness

$= 2.5 \text{ mm}$ , nominal flip angle  $= 40^\circ$ , acquisition matrix  $= 144 \times 192$ , in-plane spatial resolution  $(1.5 \times 1.5) \text{ mm}^2$ , 25 cardiac phases, TR  $= 19 \text{ msec}$ , bandwidth  $= 1030 \text{ Hz/pixel}$ , GRAPPA (R = 2)) was used. TEs were set to multiple of 1.02 msec ranging from 3.06–11.22 msec. Monoexponential fitting using nonlinear least squares optimization implemented by Trust-Region algorithm was applied for pixel-by-pixel  $T_2^*$  quantification.

For fat water separation imaging a gradient echo technique was employed (matrix size  $= 256 \times 144$ ,

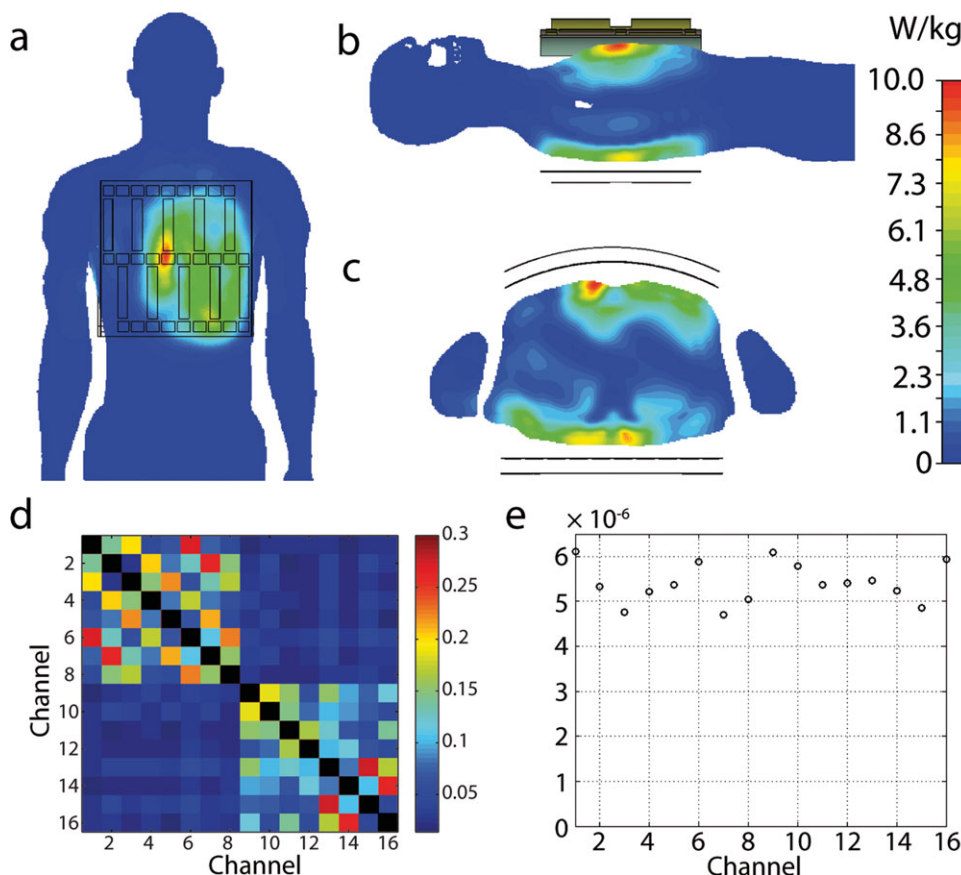


**Figure 3.** SAR distribution (local SAR, 10 g average) obtained for phase setting PS<sub>2</sub>. SAR distribution is shown for (a) the anterior surface of the voxel model, (b) a sagittal slice, and (c) a transversal slice. The slices in (b,c) were chosen to cover the region of maximum local SAR. (d) Noise correlation matrix averaged over eight subjects. (e) Noise standard deviation versus channel measured in a single subject.

slice thickness = 4 mm, receiver bandwidth = 1028 Hz/pixel bandwidth, 8 echoes acquired in 4 shots, effective echo-spacing of 0.54 msec). For water-fat separated image reconstruction a multiecho Dixon-like approach based on the VARPRO formulation with graphcut optimization (32) was applied. A volunteer study was performed in eight healthy adult male subjects (mean age 30 ± 8 years, range 25–50 years; mean body mass index [BMI] 23.3 ± 1.2, range 22–25; mean heart rate 60 ± 6 bpm, range 55–71 bpm). Informed written consent was obtained from each volunteer prior to the study in compliance with the local Institutional Review Board guidelines.

Left ventricular (LV) chamber quantification was performed in all subjects. For this a set of short-axis views of the heart ranging from the atrioventricular ring to the apex were acquired to achieve coverage of the entire left ventricle. For LV chamber quantification end-diastolic and end-systolic volume (EDV, ESV), LV ejection fraction (EF), and left ventricular mass (LVM) were obtained by manually contouring the endocardial and epicardial borders in end-diastole and end-systole using commercial software (CMR42, Circle Cardiovascular Imaging, Calgary, Canada) for all subjects. Blinded CMR reading was performed by two clinicians with expertise in clinical CMR (>3000 CMR examinations) who were not involved in the image acquisition. The overall image quality of the CINE images was rated in a blinded consensus reading of the two clinicians using a predefined scoring system. Scoring was based on blood/myocardium contrast, anatomic border sharpness, and visualization of subtle anatomic features (such as ventricular

trabeculae) using a scale ranging from 0 to 3 (0 non-diagnostic; 1 impaired image quality that may lead to misdiagnosis; 2 good; 3 excellent).

## RESULTS

### EMF and SAR Simulations

The B<sub>1</sub><sup>+</sup> distributions derived from EMF simulations agree well with the results from MR phantom

Table 1  
Phases of the Individual Coil Elements for Configurations PS<sub>1</sub> and PS<sub>2</sub>

Element number	Phase [Deg]	
	PS <sub>1</sub>	PS <sub>2</sub>
1	17	0
2	343	45
3	347	90
4	325	135
5	332	22.5
6	3	67.5
7	35	112.5
8	212	157.5
9	154	102
10	180	147
11	56	192
12	351	237
13	174	124.5
14	71	169.5
15	52	214.5
16	333	259.5

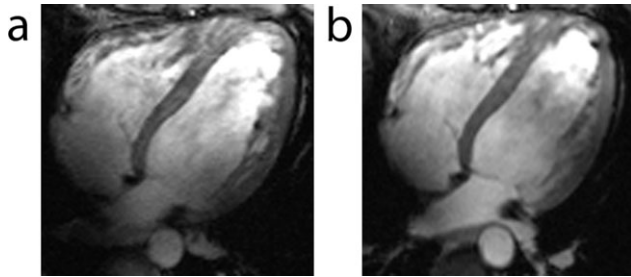


**Figure 4.** Four-chamber long-axis views of the heart derived from 2D CINE FLASH imaging using the 16-channel TX/RX coil array (in-plane resolution  $(1.4 \times 1.4) \text{ mm}^2$ , slice thickness 4 mm,  $R = 2$ , GRAPPA). Images were acquired using phase setting  $PS_1$  (a) and  $PS_2$  (b). Both configurations yielded a uniform intensity distribution and comparable overall image quality for this BMI and patient geometry.

experiments (Fig. 2). For SAR calculations the output of the RF power amplifier was limited to 30 W (6 minutes averaging time). The total mass of the voxel model is 70 kg and the exposed mass was estimated to be 30 kg. In accordance with IEC regulations (33), the limit for partial body SAR was calculated to be 6.8 W/kg. For all RF phase settings used in the volunteer studies, the partial body SAR did not exceed 0.7 W/kg, which falls well within the limits for partial body SAR. Calculations of the local SAR (10 g average) indicate that local maxima can occur inside of the body, as illustrated in Fig. 3a–c. However, these relative hotspots were found to be always below 11 W/kg, which corresponds to operation in the first level mode (maximum local SAR of 20 W/kg). Since the losses of the cables, the TX/RX switches, and the RF components were disregarded, the simulations describe a worst-

case scenario and the RF power amplifier limit of 30 W is rather conservative.

### RF Characteristics

Tuning, matching, and decoupling was performed with the coil array being loaded by a subject. The trim capacitors for decoupling of the coil elements were adjusted using the network analyzer. These settings were kept constant for all volunteers involved in the in vivo study. The reflection coefficients were below  $-16 \text{ dB}$  and the transmission coefficients were below  $-13 \text{ dB}$  for all coil elements and volunteers. The decoupling between elements of the anterior and the posterior section was below  $-30 \text{ dB}$  for all volunteers. The mean  $Q_U/Q_L$  of all 16 elements was  $4.3 \pm 1.1$ . Noise correlation was measured in vivo and averaged over all subjects. The noise correlation matrix is shown in Fig. 3d and indicates that there is rather low correlation between the channels. For the anterior section a maximum correlation of  $0.26 \pm 0.06$  was observed. For the posterior section a maximum correlation of  $0.28 \pm 0.08$  was obtained. Both values were found for a pair of next-neighboring elements. The noise standard deviation versus channel (Fig. 3e) shows that the noise is reasonably uniform.

### $B_1^+$ Homogeneity Adjustments

Two different phase settings were used for the in vivo study. For the first configuration ( $PS_1$ ) EMF simulations using the voxel model were used to reduce  $B_1^+$  inhomogeneities across the heart (18). For the second configuration ( $PS_2$ ) the first-order cp mode of the Butler matrix was used. This setting revealed a rather

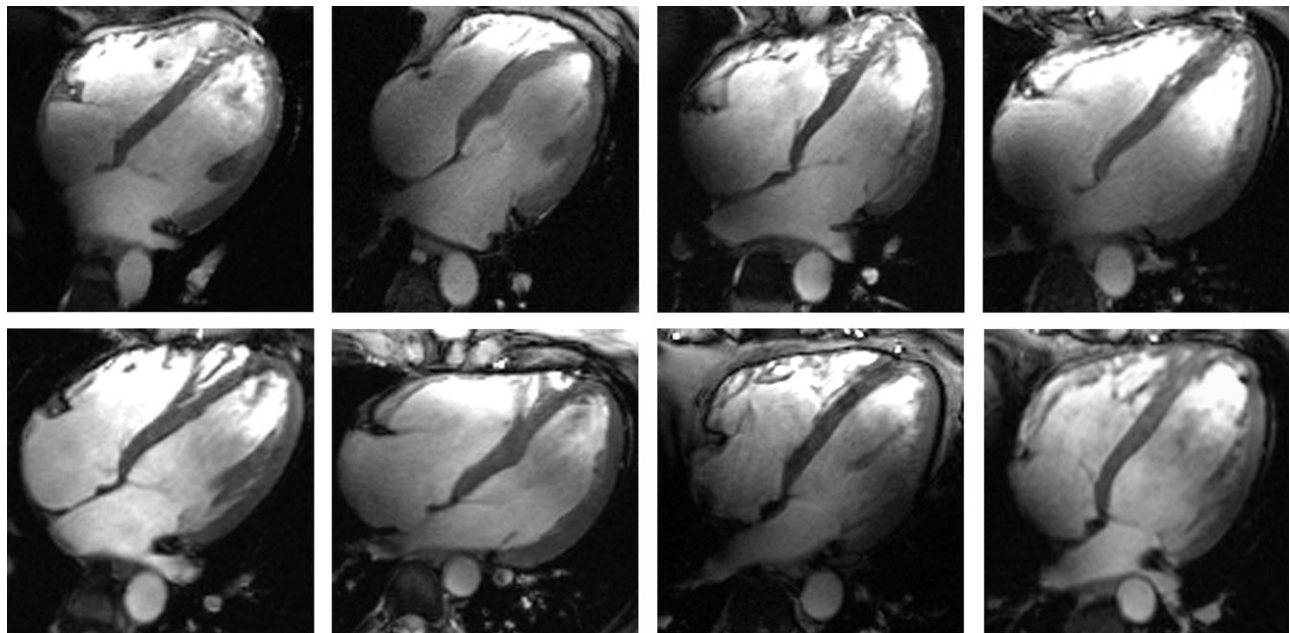


**Figure 5.** Survey of the image quality obtained within the cohort of eight volunteers. All long-axis four-chamber views were derived from 2D CINE FLASH acquisitions using the 16-channel TX/RX coil array (in-plane resolution  $(1.4 \times 1.4) \text{ mm}^2$ , slice thickness 4 mm,  $R = 2$ , GRAPPA) in conjunction with phase setting  $PS_2$  without subject-specific tuning, matching, or transmit phase adjustments.

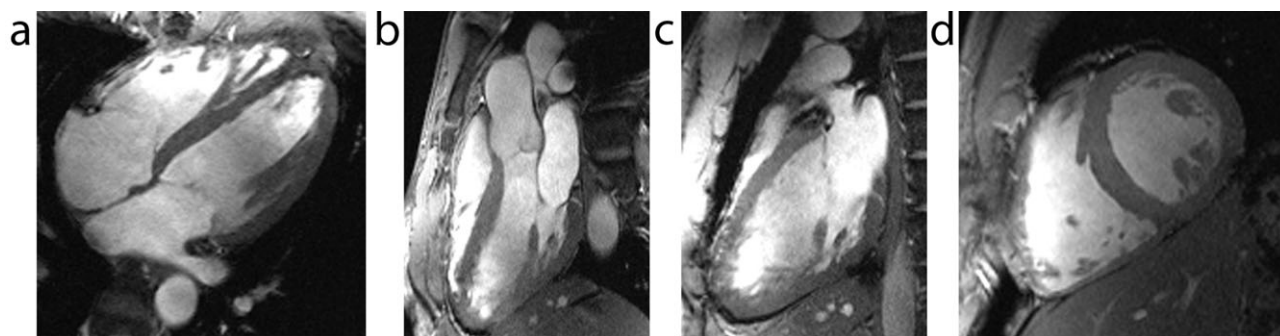


**Figure 6.** 2D CINE FLASH images acquired with the proposed 16-channel TX/RX coil array with an in-plane resolution of  $(1 \times 1) \text{ mm}^2$  (slice thickness 4 mm) using phase setting  $\text{PS}_2$  and two-fold acceleration (GRAPPA): a four-chamber view (a), a three-chamber view (b), a two-chamber view (c), and a midventricular short-axis view of the heart (d).

uniform intensity distribution with the exception of deep regions of the heart. This led to the conclusion that the phases within the anterior and superior section of the coil array were chosen appropriately. However, the phase difference between the anterior and the posterior section led to destructive interference. Hence,  $\text{PS}_2$  was modified by an additional phase shift of  $-78^\circ$  for all posterior coil elements, which was determined empirically in MR measurements. The phases of the individual elements for  $\text{PS}_1$  and  $\text{PS}_2$  are listed in Table 1.

Transmit field efficiencies of settings  $\text{PS}_1$  and  $\text{PS}_2$  were derived from the EMF simulations. Average  $B_1^+$  efficiency over an ROI encompassing a mid-axial view of the heart of the voxel model “Duke” was found to be  $4.2 \pm 2.1 \mu\text{T}/\sqrt{\text{kW}}$  ( $\text{PS}_1$ ) and  $6.5 \pm 3.1 \mu\text{T}/\sqrt{\text{kW}}$  ( $\text{PS}_2$ ). Both phase settings yielded a rather uniform intensity distribution and high myocardium/blood contrast for volunteers showing an anatomy and BMI similar to the voxel model “Duke” (Fig. 4). Image quality and blood myocardium contrast obtained for  $\text{PS}_1$  varied for volunteers not matching Duke’s anatomy and BMI. In comparison,  $\text{PS}_2$  revealed a rather constant image quality and blood myocardium contrast for all subjects investigated, as shown in Fig. 5. Consequently, only data acquired with  $\text{PS}_2$  were used for analysis of parallel imaging performance, for LV

chamber quantification, and for image quality scoring.

### Cardiac MRI

Patient preparation and total examination time did not exceed 25 minutes and hence were found in line with current clinical practice. Acquisition of stacks of 21 short-axis views covering the entire heart for LV function assessment showed a mean examination time of  $16 \pm 3$  min. All cardiac images derived from 2D CINE FLASH acquisitions using the  $\text{PS}_2$  phase setting yielded clinically acceptable image quality. The images provided rather uniform image intensity for the entire heart. This is demonstrated in Fig. 6 for standard long-axis views and in Fig. 7 for a series of short-axis views covering the heart from the apex to the base. For both sets of images the baseline SNR advantage at 7.0 T was put to use to acquire images with an in-plane resolution of  $(1 \times 1) \text{ mm}^2$  together with a slice thickness of 4 mm. This spatial resolution is superior to the spatial resolution commonly used in current clinical practice (6). The image quality derived from 2D CINE acquisitions enables the visualization of subtle anatomic structures such as pericardium, mitral, and tricuspid valves and their associated papillary muscles and trabeculae. Also, the uniform

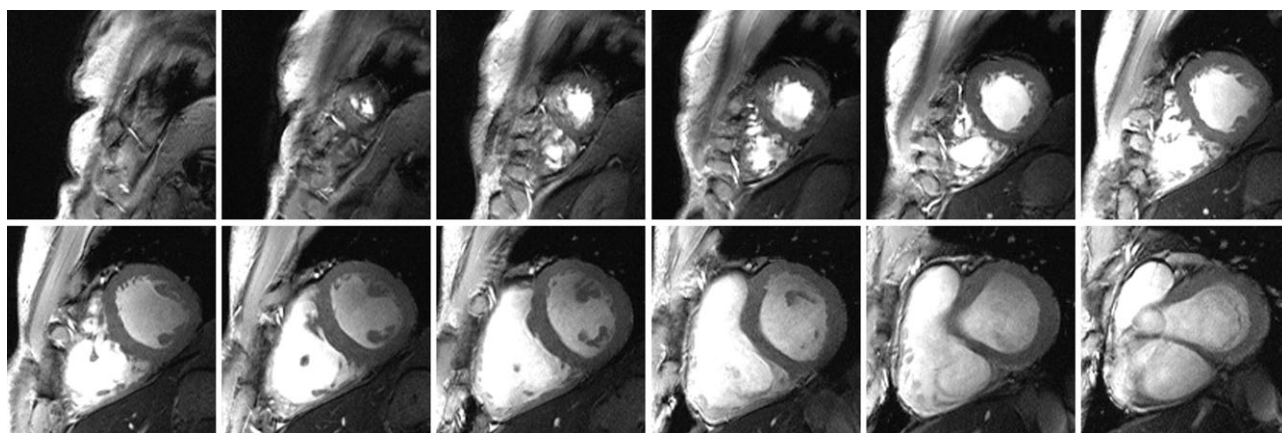


**Figure 7.** Series of 2D CINE FLASH images derived from short-axis views ranging from the apex to the base of the heart (in-plane resolution  $(1 \times 1) \text{ mm}^2$ , slice thickness 4 mm,  $R = 2$ , GRAPPA). The images illustrate that a rather uniform intensity distribution was obtained across the entire heart.

Table 2  
Results of the Analysis of SNR, CNR, and Parallel Imaging Performance

Reduction factor	R = 1	R = 2	R = 3	R = 4
SNR in LV blood pool	101 ± 19	72 ± 13	52 ± 11	40 ± 11
Blood/myocardium contrast	58 ± 35	41 ± 24	29 ± 20	19 ± 21
Average GRAPPA g-factor	—	1.10 ± 0.07	1.57 ± 0.24	2.33 ± 0.50
Maximum GRAPPA g-factor	—	1.2	2	3

intensity together with the in-plane spatial resolution and blood/myocardium CNR were found to be beneficial for visualization and delineation of cardiac structures in the right ventricle (RV).

The results of the analysis of SNR, CNR, and parallel imaging performance are shown in Table 2. SENSE-reconstructed short-axis view images obtained for reduction factors R = 1, R = 2, R = 3, and R = 4 are shown in Fig. 8. 2D CINE FLASH acquisitions using acceleration factors R = 1, R = 2, R = 3, and R = 4 together with GRAPPA reconstruction are shown in Fig. 9a. The quantitative SNR and g-factor maps derived from the datasets shown in Fig. 9a are depicted in Fig. 9b,c. SNR analysis yielded SNR = 101 ± 19 for R = 1, SNR = 72 ± 13 for R = 2, SNR = 52 ± 11 for R = 3, and SNR = 40 ± 11 for R = 4 for LV blood.

Blood/myocardium contrast was found to be 58 ± 35 (R = 1), 41 ± 24 (R = 2), 29 ± 20 (R = 3), and 19 ± 21 (R = 4). The average GRAPPA g-factors within an ROI covering the entire heart were found to be 1.10 ± 0.07 (R = 2), 1.57 ± 0.24 (R = 3), and 2.33 ± 0.50 (R = 4). The maximum g-factors were 1.2 (R = 2), 2 (R = 3), and 3 (R = 4) for all subjects.

The mean results of the LV chamber quantification were: EDV = 150.7 ± 36.5 mL, ESV = 61.2 ± 16.0 mL, EF = 59.0 ± 2.7%, and LVM = 104.1 ± 25.6 g. The image quality score averaged over all eight subjects was 2.4 ± 0.2 with the lowest score at 2.15.

The proposed RF coil was also employed in CMR applications other than LV function assessment. This includes the assessment of the RV. Figure 10a,b shows a long-axis and a four-chamber view of the RV using a spatial resolution of (1.4 × 1.4 × 4.0) mm<sup>3</sup>. The uniform intensity together with the in-plane spatial resolution and blood/myocardium CNR were found to be beneficial for visualization and delineation of cardiac structures in the RV. Subtle anatomic RV structures, such as the valvular apparatus and RV trabeculae, were accurately identifiable. This approach offers the potential to gain a better insight into the morphology and function of the RV and may help to enhance the detection of small wall motion abnormalities.

Because of the super-linear relationship between magnetic field strength and microscopic B<sub>0</sub> inhomogeneities (34) it is conceptually appealing to pursue susceptibility weighted myocardial imaging at 7.0 T which aims at parametric mapping for non-invasive tissue characterization. Here, the sensitivity and parallel imaging performance of the coil was put to use to accomplish breath-held T<sub>2</sub>\* mapping of the heart. Figure 10c shows a T<sub>2</sub>\* map for the left ventricle using slices as thin as 2.5 mm and an in-plane spatial resolution of (1.5 × 1.5) mm<sup>2</sup> to reduce dephasing due to macroscopic B<sub>0</sub> inhomogeneities, such as the lung/heart interface.

Figure 10d demonstrates that the proposed coil supports fat-water separated cardiac CINE imaging at 7.0 T using a multiecho Dixon-like approach (32,35), which provides a sensitive means for tissue characterization and suppression of bright fat signal that may otherwise obscure the water signal of interest (36). Fat and water were correctly classified and good separation was achieved across the full FOV. Fat suppression was estimated in water regions to be greater than 30:1 across the FOV.

## DISCUSSION

This technical development study demonstrates the feasibility of CMR imaging at 7.0 T using a dedicated, 2D TX/RX coil array that uses loop elements and that provides image quality suitable for clinical use, patient comfort, and ease of use. The results derived from RF characteristics and noise correlation assessment are encouraging and suggest that subject-specific tuning and matching may not be essential when using the proposed 16-channel coil array in a clinical setting. The 2D CINE FLASH acquisitions provided a rather constant image quality for the BMI range involved in this study without individual adjustments of the RF coil transmit phases. This led to an acceptable preparation and examination time that meets the needs of a clinical setting. The application of the proposed coil for breath-held myocardial T<sub>2</sub>\* mapping and

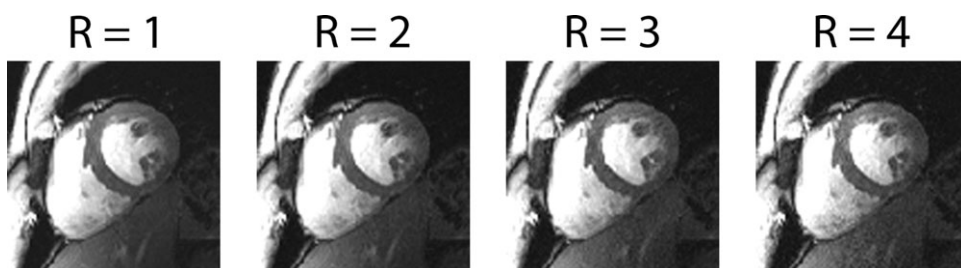
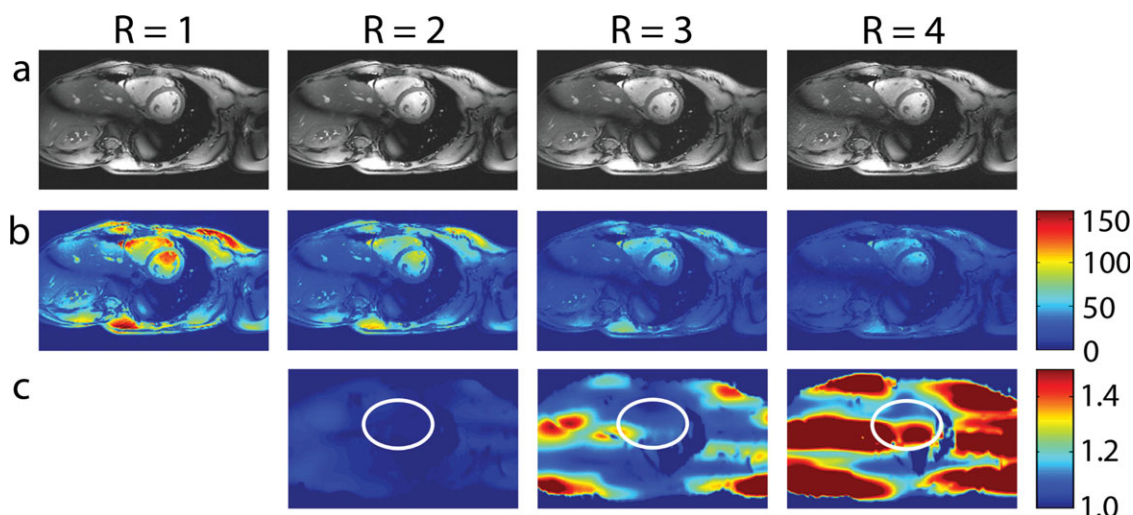


Figure 8. 2D CINE FLASH images of a midventricular short-axis view at diastole (in-plane resolution (1.4 × 1.4) mm<sup>2</sup>, slice thickness 4 mm) using reduction factors R = 1 (no reduction), R = 2, R = 3, and R = 4 together with off-line SENSE reconstruction.



**Figure 9.** (a) 2D CINE FLASH images of a midventricular short-axis view at diastole (in-plane resolution  $(1.4 \times 1.4) \text{ mm}^2$ , slice thickness 4 mm) using reduction factors  $R = 1$  (no reduction),  $R = 2$ ,  $R = 3$ , and  $R = 4$  together with GRAPPA reconstruction. (b) Quantitative SNR maps derived from the datasets in (a). (c) Calculated g-factor maps derived from the datasets shown in (a). The elliptical ROI across the heart which was used for the estimation of the mean g-factor and its standard deviation is depicted in white.

fat-water separation imaging of the heart at 7.0 T was also shown. RF transmission configurations with more than two independent channels are not readily available in clinical or preclinical MR yet. Our approach, which uses a single feeding transmit channel in conjunction with a power splitter and a fixed phase setting, can be made easily available for a large number of MR sites. Although this  $B_1^+$  calibration concept might not work perfectly for all body geometries and BMIs, our results indicate that clinically acceptable image quality can be obtained for a common range of BMIs without the need of patient-specific adjustments. This helps to accomplish examination times at 7 T that match those reported for LV function assessment in clinical routine using 1.5 T and 3.0 T systems (2). If patient-specific  $B_1^+$  shimming and extra coil adjustments are applied, averaged total examination

times are substantially prolonged and can lengthen toward averaged scan times of 93 minutes (2), which exceeds what is clinically acceptable. Long scan times exhibit a limited compatibility with the concept of a 15–30-minute dedicated cardiac MR examination that includes assessment of global function but also other applications like myocardial perfusion, myocardial viability, and coronary artery vessel assessment. To this end we anticipate expanding our work to rapid subject-specific  $B_1^+$  shimming (12,37) routines with the ultimate goal to maintain image quality shown here for BMIs far beyond those used in our initial volunteer study without exceeding clinically acceptable scan times.

The inherent SNR benefit of UHF MR together with the SNR advantage of a closely fitting cardiac coil were transferred into high spatial resolution 2D CINE

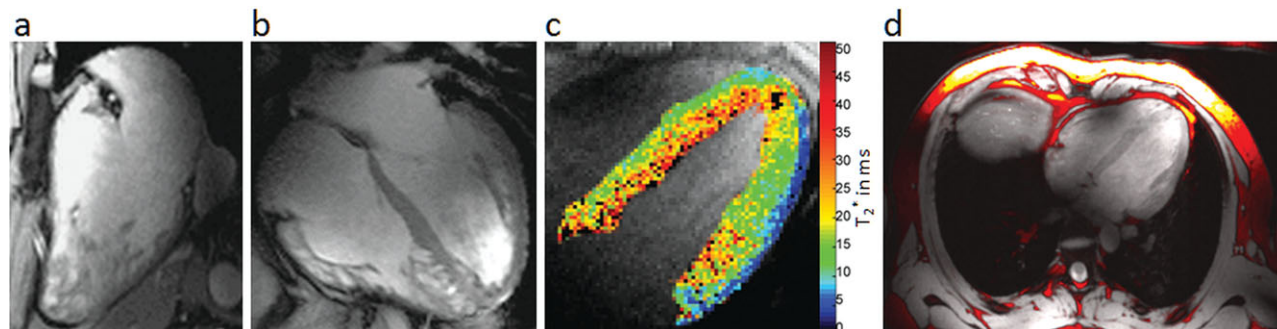


**Figure 10.** Long axis (a) and axial (b) view of the RV derived from 2D CINE FLASH acquisitions using the 16-element TX/RX coil and a spatial resolution of  $(1.4 \times 1.4 \times 4.0) \text{ mm}^3$ . Subtle anatomic RV structures, such as the valvular apparatus and RV trabeculae, are identifiable.  $T_2^*$  map (c) of the LV obtained from prospectively triggered spoiled 2D gradient echo acquisitions (slice thickness = 2.5 mm, in-plane spatial resolution  $(1.5 \times 1.5) \text{ mm}^2$ ). Combined fat (red scale) plus water (gray scale) image (d) of a healthy subject acquired at 7.0 T using a gradient echo technique together with the proposed 16-channel TX/RX coil. Fat and water were correctly classified and good separation was achieved across the full FOV. Fat suppression was estimated in water regions to be greater than 30:1 across the FOV.

FLASH cardiac function imaging using the 16-channel TX/RX coil array. 2D CINE FLASH acquisitions provided rather uniform intensities across the heart including standard cardiac views used in clinical practice. The increased SNR at 7.0 T can be transferred into an enhanced in-plane spatial resolution. The proposed coil array supports 1D accelerations of up to  $R = 4$  without significantly impairing image quality.

Parallel imaging techniques provide scan accelerations required for large-volume 3D acquisitions. The maximum possible acceleration increases with increasing the number of array elements. Multidimensional RF coil arrays are capable of multidimensional accelerations, which serve to reduce noise amplification inherent in parallel imaging and hence preserve SNR as compared to 1D accelerations (20,38). Previous studies have shown that 3D volumetric acquisitions also serve to recover SNR via noise averaging (39,40). Hence, we anticipate examining the array's capabilities for volumetric acquisitions, which is beyond the scope of the current work.

Recognition of the benefits and performance of 2D local surface coil arrays shown here might result in a migration to 3.0 T, where the RF inhomogeneity effects for CMR encountered in routine clinical imaging, although somewhat reduced, remain significant. The improved  $B_1$  efficiency of local TX/RX coil arrays bears the potential to address RF power deposition and imaging speed constraints frequently encountered in current clinical practice at 3.0 T when using the body coil for excitation. The transmission  $B_1$  efficiency advantage can be translated into a shortening of RF pulses which could afford a reduction in TE and TR for 2D CINE SSFP imaging—the gold standard for cardiac chamber quantification and LV assessment. A decrease in TR would be helpful for LV assessment at 3.0 T, where the use of steady-state free precession (SSFP) is limited by susceptibility-induced off-resonance effects, resulting in either SSFP banding artifacts across the heart or the need to use short TRs that limit the readout matrix size and hence the spatial resolution achievable in current clinical practice.

Our study, while important, indicates the need for additional studies including 2D TX/RX coil arrays with more than 16 elements. This approach would help to break ground for transmit whole-body arrays at 7.0 T and hence would be beneficial not only for CMR but also for body imaging and other large volume MRI applications. It is a recognized limitation of this technical development study that only 1D accelerations were used for parallel imaging and that only a limited BMI range was involved.

To conclude, we have shown that the designed 16-channel cardiac transeiver coil has the capability to acquire high contrast, high spatial resolution images of the heart at 7.0 T. The RF penetration seems sufficient for healthy subjects.  $B_1^+$  nonuniformities can be mitigated with appropriate  $B_1^+$  phase settings. The results underline the challenges of CMR at 7.0 T and demonstrate that these issues can be offset by using tailored RF hardware and methodology. The benefits of such improvements would be in positive alignment

with the clinical needs of an ever-growing spectrum of indications for CMR.

## REFERENCES

- Hundley WG, Bluemke DA, Finn JP, et al. ACCF/ACR/AHA/NASCI/SCMR 2010 expert consensus document on cardiovascular magnetic resonance: a report of the American College of Cardiology Foundation Task Force on Expert Consensus Documents. *Journal of the American College of Cardiology* 2010;55:2614.
- Suttie JJ, Delabarre L, Pitcher A, et al. 7 Tesla (T) human cardiovascular magnetic resonance imaging using FLASH and SSFP to assess cardiac function: validation against 1.5 T and 3 T. *NMR Biomed* 2012;25:27-34.
- Vaughan JT, Snyder CJ, DelaBarre LJ, et al. Whole body imaging at 7T: preliminary results. *Magn Reson Med* 2009;61:244-248.
- Snyder CJ, DelaBarre L, Metzger GJ, et al. Initial results of cardiac imaging at 7 Tesla. *Magn Reson Med* 2009;61:517-524.
- van Elderen SG, Versluis MJ, Webb AG, et al. Initial results on in vivo human coronary MR angiography at 7 T. *Magn Reson Med* 2009;62:1379-1384.
- von Knobelsdorff-Brenkenhoff F, Frauenrath T, Prothmann M, et al. Cardiac chamber quantification using magnetic resonance imaging at 7 Tesla—a pilot study. *Eur Radiol* 2010:1-9.
- Niendorf T, Sodickson DK, Krombach GA, Schulz-Menger J. Toward cardiovascular MRI at 7 T: clinical needs, technical solutions and research promises. *Eur Radiol* 2010:1-11.
- van Elderen SG, Versluis MJ, Westenberg JJ, et al. Right coronary MR angiography at 7 T: a direct quantitative and qualitative comparison with 3 T in young healthy volunteers. *Radiology* 2010;257:254-259.
- Schick F. Whole-body MRI at high field: technical limits and clinical potential. *Eur Radiol* 2005;15:946-959.
- Frauenrath T, Hezel F, Heinrichs U, et al. Feasibility of cardiac gating free of interference with electro-magnetic fields at 1.5 Tesla, 3.0 Tesla and 7.0 Tesla using an MR-stethoscope. *Invest Radiol* 2009;44:539.
- Frauenrath T, Hezel F, Renz W, et al. Acoustic cardiac triggering: a practical solution for synchronization and gating of cardiovascular magnetic resonance at 7 Tesla. *J Cardiovasc Magn Reson* 2010;12:1-14.
- Van de Moortele PF, Akgun C, Adriany G, et al.  $B_1$  destructive interferences and spatial phase patterns at 7 T with a head transeiver array coil. *Magn Reson Med* 2005;54:1503-1518.
- Yang QX, Wang J, Zhang X, et al. Analysis of wave behavior in lossy dielectric samples at high field. *Magn Reson Med* 2002;47:982-989.
- Vaughan JT. High frequency coils. In: Robitaille PL, Berliner LJ, editors. *Ultra high field magnetic resonance imaging and spectroscopy*. New York: Springer; 2006. p 127-161.
- Maderwald S, Orzada S, Schaefer LC, et al. 7T human in vivo cardiac imaging with an 8-channel transmit/receive array. In: *Proc 17th Annual Meeting ISMRM, Honolulu; 2009 (abstract 822)*.
- Versluis MJ, Tsekos N, Smith NB, Webb AG. Simple RF design for human functional and morphological cardiac imaging at 7Tesla. *J Magn Reson* 2009;200:161-166.
- Dieringer M, Renz W, Lindel T, et al. Design and application of a four channel transmit/receive surface coil for functional cardiac imaging at 7T. *J Magn Reson Imaging* 2011;33:736-741.
- Gräßl A, Winter L, Thalhammer C, et al. Design, evaluation and application of an eight channel transmit/receive coil array for cardiac MRI at 7.0 T. *Eur J Radiol* 2011 [Epub ahead of print].
- Adriany G, Ritter J, Vaughan JT, Ugurbil K, Moortele PF. Experimental verification of enhanced  $B_1$  shim performance with a Z-encoding RF coil array at 7 Tesla. In: *Proc Joint Annual Meeting ISMRM-ESMRMB, Stockholm; 2010 (abstract 3831)*.
- Ohliger MA, Grant AK, Sodickson DK. Ultimate intrinsic signal-to-noise ratio for parallel MRI: electromagnetic field considerations. *Magn Reson Med* 2003;50:1018-1030.
- Wiesinger F, Boesiger P, Pruessmann KP. Electrodynamics and ultimate SNR in parallel MR imaging. *Magn Reson Med* 2004;52:376-390.
- Niendorf T, Hardy CJ, Giaquinto RO, et al. Toward single breath-hold whole-heart coverage coronary MRA using highly accelerated

- parallel imaging with a 32-channel MR system. *Magn Reson Med* 2006;56:167–176.
23. Vaughan JT, Snyder C, DelaBarre L, et al. RF coil designs for 7T cardiac imaging. In: *Proc Joint Annual Meeting ISMRM-ESMRMB*, Stockholm; 2010 (abstract 49).
  24. Raaijmakers AJ, Ipek O, Klomp DW, et al. Design of a radiative surface coil array element at 7 T: the single-side adapted dipole antenna. *Magn Reson Med* 2011;66:1488–1497.
  25. Wald LL, Wiggins GC. New coil systems for highly parallel MR acquisition strategies. In: Schoenberg SO, Dietrich O, Reiser MF, editors. *Parallel imaging in clinical MR applications*. Berlin-Heidelberg: Springer; 2007. p 497–510.
  26. Butler J. Beam-forming matrix simplifies design of electronically scanned antennas. *Electron Des* 1961;9:170–173.
  27. Christ A, Kainz W, Hahn EG, et al. The virtual family—development of surface-based anatomical models of two adults and two children for dosimetric simulations. *Phys Med Biol* 2010;55:N23.
  28. Kozlov M, Turner R. Fast MRI coil analysis based on 3-D electromagnetic and RF circuit co-simulation. *J Magn Reson* 2009;200:147–152.
  29. Akoka S, Franconi F, Seguin F, Le Pape A. Radiofrequency map of an NMR coil by imaging. *Magn Reson Imaging* 1993;11:437–441.
  30. Frauenrath T, Niendorf T, Kob M. Acoustic method for synchronization of magnetic resonance imaging (MRI). *Acta Acustica United with Acustica* 2008;94:148–155.
  31. Kellman P, McVeigh ER. Image reconstruction in SNR units: a general method for SNR measurement. *Magn Reson Med* 2005;54:1439–1447 (erratum: *Magn Reson Med* 2007;58:211–212).
  32. Hernando D, Kellman P, Haldar JP, Liang ZP. Robust water/fat separation in the presence of large field inhomogeneities using a graph cut algorithm. *Magn Reson Med* 2010;63:79–90.
  33. IEC. 60601–2–33 Medical electrical equipment. Part 2–33: Particular requirements for the basic safety and essential performance of magnetic resonance equipment for medical diagnosis. Edition 3.0; 2010.
  34. Turner R, Jezzard P, Wen H, et al. Functional mapping of the human visual cortex at 4 and 1.5 Tesla using deoxygenation contrast EPI. *Magn Reson Med* 1993;29:277–279.
  35. Reeder SB, Markl M, Yu H, Hellinger JC, Herfkens RJ, Pelc NJ. Cardiac CINE imaging with IDEAL water-fat separation and steady-state free precession. *J Magn Reson Imaging* 2005;22:44–52.
  36. Kellman P, Hernando D, Arai AE. Myocardial fat imaging. *Curr Cardiovasc Imaging Rep* 2010;3:83–91.
  37. Brunner DO, Pruessmann KP. B 1+ interferometry for the calibration of RF transmitter arrays. *Magn Reson Med* 2009;61:1480–1488.
  38. Weiger M, Pruessmann KP, Boesiger P. 2D SENSE for faster 3D MRI. *Magn Reson Mater Phys* 2002;14:10–19.
  39. Zhu Y, Hardy CJ, Sodickson DK, et al. Highly parallel volumetric imaging with a 32-element RF coil array. *Magn Reson Med* 2004;52:869.
  40. Sodickson DK, Hardy CJ, Zhu Y, et al. Rapid volumetric MRI using parallel imaging with order-of-magnitude accelerations and a 32-element RF coil array. Feasibility and implications. *Acad Radiol* 2005;12:626–635.